Quantum Nanophotonic Interface for Tin-Vacancy Centers in Thin-Film Diamond

Hope Lee,^{1,*} Hannah C. Kleidermacher,^{1,*} Abigail J.M. Stein,^{1,*} Hyunseok Oh,² Lillian B. Hughes Wyatt,³ Casey K. Kim,³ Luca Basso,⁴ Andrew M. Mounce,⁴ Yongqiang Wang,⁵ Shei S. Su,⁴ Michael Titze,^{4,6} Ania C. Bleszynski Jayich,² and Jelena Vučković^{1,†}

⁵Los Alamos National Laboratory, Los Alamos, New Mexico 87525, USA

The negatively charged tin-vacancy center in diamond (SnV⁻) is an excellent solid state qubit with optically-addressable transitions and a long electron spin coherence time at elevated temperatures. However, implementing scalable quantum nodes with high-fidelity optical readout of the electron spin state requires efficient photon emission and collection from the system. In this manuscript, we report a quantum photonic interface for SnV⁻ centers based on one-dimensional photonic crystal cavities fabricated in diamond thin films. Furthermore, we develop a model describing the spontaneous emission dynamics of our system, allowing for rigorous determination of Purcell factors and the C/D branching ratio from cavity enhancement of the C and D transitions of the SnV⁻ zero phonon line. We observe quality factors up to ~6000 across this sample, and measure up to a 12-fold lifetime reduction. By considering the lifetime reduction of both the C and D transitions independently, we determine the C/D branching ratio to be $\eta_{\rm BR}=0.7815$, in line with previous theoretical and experimental findings. Finally from our analysis, we extract a Purcell factor of up to $F_C=26.21\pm0.01$ for a single SnV⁻ transition.

I. INTRODUCTION

Optically-active defects in semiconductors, or color centers, are a leading platform for quantum network qubits due to their long spin coherence times, bright optical emission, and native compatibility with nanophotonic integration [1–3]. Although the initial keystone quantum network demonstrations utilized the nitrogen vacancy (NV⁻) center in diamond [4, 5], negatively charged group-IV color centers in diamond have garnered interest due to their first-order insensitivity to electric field noise and increased fraction of coherent emission into the zero phonon line (ZPL) [6]. These features render the group-IV vacancy centers significantly more compatible with nanophotonic integration, which is required for downstream scaling of multiple quantum network nodes. The most mature of this family of color centers is the negatively charged silicon vacancy center (SiV⁻), which has enabled long-distance networking demonstrations on the scale of those achieved with NV⁻ centers [7]. However, the SiV suffers from a limited ground state splitting of ~ 50 GHz, necessitating either mK dilution refrigerator environments or diligent strain engineering for spin state control. In contrast, the rapidly maturing tin-vacancy (SnV⁻) maintains spin coherence at liquid helium temperatures, around 1.7 K, due to its significantly larger ground state splitting of ~ 850 GHz [8, 9].

The tin-vacancy has similarly demonstrated its suitability as a qubit for long distance quantum networks with high fidelity initialization, manipulation, and readout of the qubit spin states and coupling to nanophotonic devices [9–12]. However, photonic interfaces for the SnV⁻ have thus far been fabricated via diamond bulk carving techniques [13, 14], severely limiting device performance, fabrication yield, and feasibility of integration with other photonic and electronic components on-chip. Thus the adoption of thin-film diamond paves the way for scalable quantum networks [15–17].

In this manuscript, we report the fabrication of 1D photonic crystal cavity nanobeams with quality factors of up to ~ 6000 . In particular, we fabricated two orientations of cavity devices, one parallel to and one at $\sim 55^{\circ}$ to the $\langle 100 \rangle$ axis of the diamond lattice. We measure, for each cavity orientation ('parallel' and 'angled') the lifetime reduction of two zero phonon line (ZPL) transitions (C and D) for a SnV- color center. These transitions have the same spatial positioning in the cavity field, but orthogonally polarized dipole moments. The ratio of the C to D transition emission rates is referred to as the branching ratio [6, 14, 18]. The conventional figure of merit for color center-cavity coupling is the Purcell factor, defined as the enhancement in spontaneous emission rate for a particular transition when on resonance with the cavity mode. In previous reports, Purcell factors were calculated via applying lump-sum correction factors to the measured lifetime reduction ratio without consideration of the individual transitions [12, 13]. To determine our Purcell factors with a more rigorous treatment, we construct a model to describe the spon-

 ¹ Edward L. Ginzton Lab, Stanford University, Stanford, California 94305, United States
 ² Department of Physics, University of California, Santa Barbara, California 93106, USA
 ³ Materials Department, University of California, Santa Barbara, California 93106, USA
 ⁴ Sandia National Laboratories, Albuquerque, New Mexico 87123, USA

⁶Advanced Instrumentation for Nano-Analytics, Luxembourg Institute of Science and Technology, Belvaux, L-4422 Luxembourg (Dated: November 11, 2025)

^{*} These authors contributed equally to this work.

[†] jela@stanford.edu

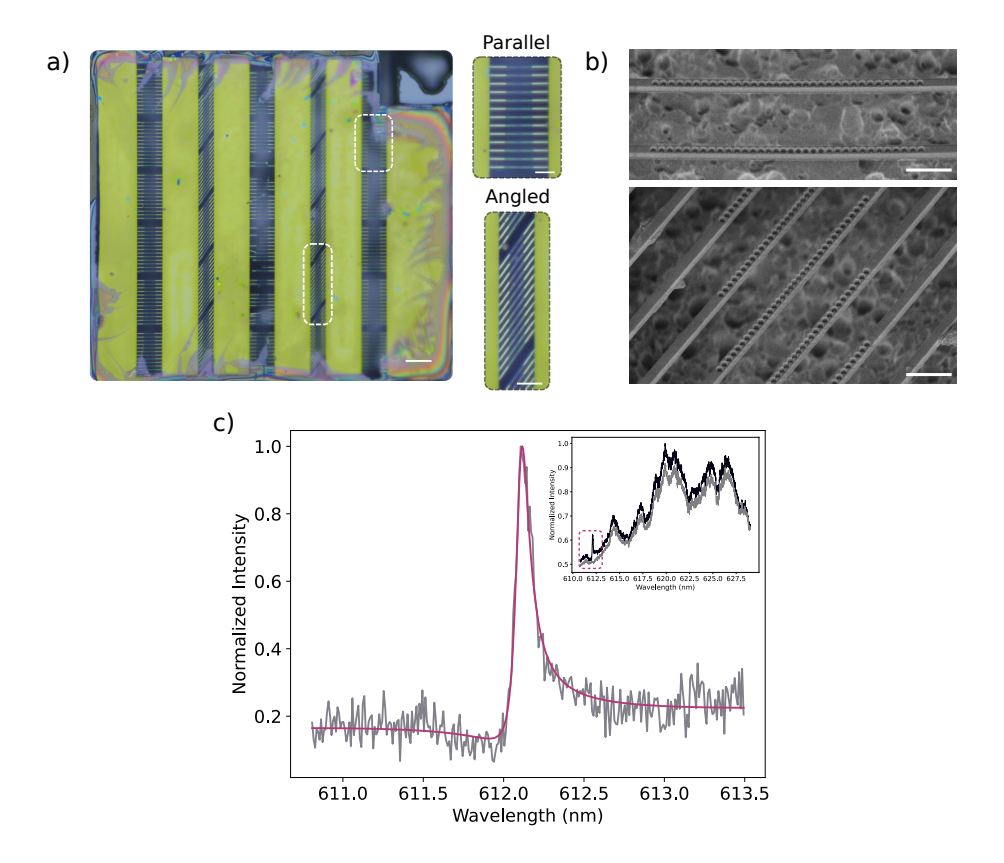


FIG. 1. Cavity design, fabrication, and characterization. (a) A white light image of the fabricated devices on the thin film membrane. Representations of the two classes of devices, parallel and angled, are indicated by the white dashed boxes and zoomed to be shown in greater detail. The scale bars indicate $15 \mu m$ and $5 \mu m$ for the zoomed out and in images, respectively. (b) SEM of fabricated devices. Scale bars indicate $1\mu m$. (c) The cross polarized reflectivity spectrum for the parallel device. The broadband spectrum is background corrected, then fit to a Fano model, yielding a quality factor of 6032. The inset shows the broadband reflectivity spectra for both the resonance and background. The fitted region is indicated by the dashed box.

taneous emission dynamics of our system which takes both C/D transitions into account. From this model, we analytically determine the C/D transition branching ratio to be $\eta_{BR} = 0.7815$, in agreement with previous reports [6, 14, 18]. Ultimately, we report the highest Purcell factor observed for this set of measurements to be $F_C = 26.21 \pm 0.01$ for the C transition in the angled device, for which the cavity mode and dipole emission are best aligned out of the available dipole-cavity orientation combinations. Indeed, our analysis highlights that aligning the photonic crystal cavity at 45° from the diamond $\langle 100 \rangle$ crystal axis would result in the highest possible improvement in Purcell factor ($\sim 40\%$) for either the C or D transition of a coupled SnV⁻ center. These results constitute crucial progress towards the implementation of scalable quantum networks based on the SnV⁻.

II. RESULTS

A. Device Design and Fabrication

Thin film diamond was prepared via the procedures outlined in [16]. $\mathrm{Sn^{2+}}$ was implanted into the bulk sample prior to membrane exfoliation with an implantation energy of 380 keV and at a dose of 2×10^{11} ions/cm², targeting $\mathrm{SnV^{-}}$ formation $\sim\!90$ nm below the surface. Final membrane thicknesses were tuned to 180 nm by reactive ion etching.

Photonic crystal cavities were designed with a 300 nm beam width and 115 nm diameter holes etched into the diamond film. The mirror reflectors consist of 10 holes on each side, while the central cavity consists of 12 holes, with quadratically tapered lattice spacings. In order to account for fabrication infidelities and ensure resonances in proximity of the $\rm SnV^-$ 619 nm ZPL wavelength, we sweep the lattice spacings from 180 nm to 210 nm in steps of 2.5 nm per device.

For the cavities reported in this manuscript, we measure a post-fabrication beam width of 326 ± 13 nm, average hole diameter of 134 ± 3 nm, and lattice constant

of 210 nm for the parallel device; and a beam width of 325 ± 2 nm, average hole diameter of 119 ± 4 nm, and lattice constant of 197.5 nm for the angled device, determined via SEM (Fig. 1b). We note that our etch recipe renders a $\sim 5-10^\circ$ sidewall angle. Taking these dimensions into account, we simulate quality factors (Q) of 2.8×10^5 (2.3×10^4) and mode volume (V) 0.46 (0.46) ($\frac{\lambda}{n}$)³ for the parallel (angled) device. Further discussion of device design and fabrication yield is provided in Appendix A 3.

Additional thin film and device fabrication details are provided in Appendix A 1 and A 2. In order to optimize space usage of the limited diamond film, transmission access for photonic crystals was forgone and instead all devices were probed out of plane.

B. Characterization of Devices and Color Centers

Our sample is maintained at 4 K in a Montana Instruments closed cycle cryostat. We utilize two discrete optical paths, subsequently referred to as the i) 'crosspolarized' and ii) photoluminescence ('PL') paths. The two optical paths enable independent access to the cavity resonance and color center signals. The optical setup is described in greater detail in Appendix B. We start by probing our cavity resonances using the cross-polarized reflectivity path. The cavities are mounted such that the resonance modes for parallel devices are primarily vertically polarized (the fundamental mode polarization is orthogonal to the cavity axis). Devices are excited via a horizontally polarized, broadband supercontinuum laser, and the vertically polarized, reflected signal is collected by a spectrometer. A half-wave plate (HWP) inserted in the shared excitation and collection path is used to optimize the SNR of the reflected cavity signal, as different HWP settings are required for parallel versus angled devices. Each broadband reflectivity spectrum is background-corrected and then fit to a Fano model. For the parallel device, we determine a quality factor of 6032 (Fig. 1c). The quality factor of the angled device was determined to be 3942, as discussed in Appendix D 2. Fig. 12).

1. PL enhancement

Next, we perform photoluminescence (PL) spectroscopy to identify emitters located in the cavity mode, exciting with ~ 5 mW of a 520 nm CW source and filtering collected counts with a 620/14 nm bandpass filter (Fig. 2b). Due to the high implantation density, approximately 2-3 emitters lie within our cavity mode. To probe for emitter-cavity coupling, we first red-shift the cavity resonance past the identified SnV⁻ transitions via argon gas condensation. Then, we 'back-tune' the resonance controllably by illuminating the nanobeam with ~ 0.75 mW of green excitation power to evaporate con-

densed gmas, while simultaneously collecting PL spectra to characterize SnV^- PL enhancement (Fig. 2c). For the parallel device, we identify a ~ 10 -fold PL enhancement of the emitter when the cavity is tuned into resonance with the transition (Fig. 2d). This measure of PL enhancement indicates significant emitter-cavity coupling, but does not suffice as an accurate measure of the Purcell factor given uncertainties in exact collection efficiencies. PL enhancement measurements for the angled device are provided in Appendix D 2.

2. Lifetime reduction measurement and calculation

To quantify Purcell factors, we measure the lifetime reduction of the emitter when the cavity is tuned into resonance. As before, we red-detune the cavity resonance beyond the SnV⁻ transition in preparation for a backtuning sweep across the target wavelength. However, we now toggle our excitation between the cross polarized path, used to both monitor and back-tune the resonance wavelength, and the PL path, used to measure the emitter optical lifetime. In the PL path, we isolate a single transition with a narrow band (~ 0.3 nm) tunable filter, and excite the emitter above band with a 520 nm pulsed laser. We apply excitation pulses with 16 ns pulse widths, a 3.3 MHz repetition rate and an averaged power of 270 μ W. In the cross polarized path, we excite simultaneously with both the supercontinuum and CW green diode laser (set again to ~ 0.75 mW) in order to both monitor and backtune the cavity resonance. Each lifetime trace is integrated for 3 minutes to build up suitable count rates, while each cross-polarized resonance spectrum is integrated for 3 seconds to allow ample time for the cavity resonance to gradually back-tune across the transition.

We target selective collection from the C transition, but due to collective emission dynamics, we see significant lifetime reduction when the cavity is on resonance with either the C or D transition individually. Furthermore, we will show in Section IIB3 that by considering the orthogonality of the C and D dipoles, we can extract the C/D branching ratio and individual Purcell factors for each transition. In preparation for this analysis, we calculate the spontaneous emission rate from the measured emitter decay lifetime via $\Gamma = 1/\tau_{\text{lifetime}}$. When resonant with the cavity, transition C(D) demonstrates a lifetime of 1.847 ± 0.002 ns, or emission rate 0.543 1/ns $(4.570 \pm 0.02 \text{ ns}, \text{ or emission rate } 0.219 \text{ 1/ns})$ compared to the off-resonance lifetime of 9.412 ± 0.09 ns, or emission rate 0.106 1/ns (Fig. 3c). We then fit the data to a double Lorentzian model. Dividing the fitted Lorentzian amplitude to the background yields a the emission rate enhancement ratio, which we denote as ζ . For the C and D transitions, we extract $\zeta_C = 4.672$ and $\zeta_D = 1.985$, respectively (Fig. 3a).

For the angled device, there remain contributions from a secondary emitter in the collected counts. We there-

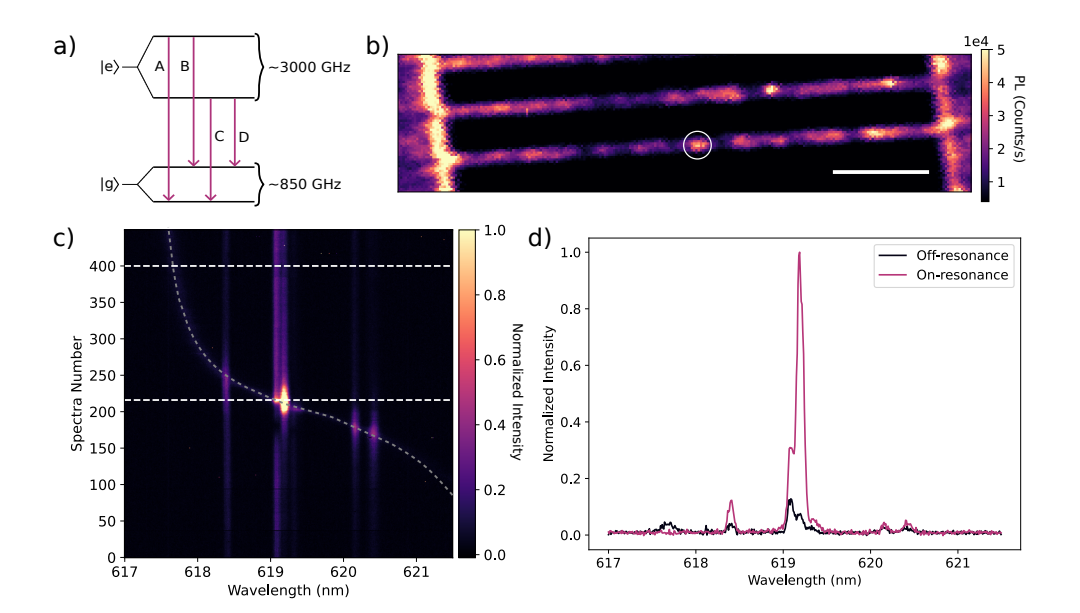


FIG. 2. SnV^- level structure, PL confocal scan and cavity enhancement. (a) Schematic of the orbital energy states of the SnV^- . Characteristic of a group-IV color center, the ground $(|g\rangle)$ and exited state $(|e\rangle)$ are split via the combined effects of spin-orbit coupling and the Jahn-Teller effect. For the SnV^- the ground state splitting is ~ 850 GHz, and the excited state splitting ~ 3000 GHz; these state splittings yield four separate ZPL transitions. In cryogenic conditions, PL signal is dominated by the two longer wavelength, lower energy transitions, labeled as C and D [19]. (b) PL confocal scan of the parallel device. The emitter cluster addressed is indicated by the white circle. The scale bar indicates $3\mu\mathrm{m}$. (c) PL enhancement via gas tuning. The cavity resonance is first red-shifted via Ar gas condensation past all SnV^- transitions of interest. The sample is then naturally 'back-tuned' over the course of repeated PL scans. The two spectra of interest are indicated by the white dashed lines. The gray dashed line is an approximate guide for the eye of the cavity resonance. (d) PL spectra on and off resonance with the cavity. We see that the most strongly enhanced SnV^- transition demonstrates a ~ 10 -fold PL enhancement.

fore fit the spontaneous emission rates to a quadruple Lorentzian model. We determine that transition C(D) demonstrates a lifetime of 1.079 \pm 0.002 ns , or emission rate 0.926 1/ns (8.109 \pm 0.2 ns, or emission rate 0.123 1/ns) compared to the off-resonance lifetime of 10.507±0.2 ns, or emission rate 0.095 1/ns (Fig. 3d). The fitted amplitude ratios are $\zeta_C=12.230$ and $\zeta_D=1.514$ (Fig. 3b).

3. Purcell factor analysis

From lifetime reduction measurements of the C and D transitions when each is resonant with the cavity, one can extract both the branching ratio and the respective Purcell factors associated with each transition. We further substantiate these analyses by comparing the interactions of emitters coupled to the parallel and angled devices and illustrate how our measured values are consistent with the known angular offsets of the emitter and the designed devices with respect to the crystallographic lattice.

We express the spontaneous emission dynamics of the full cavity-emitter system with the following expressions for spontaneous emission rates:

$$\Gamma_0 = \Gamma_C + \Gamma_D + \gamma_{PSB} \tag{1}$$

$$\Gamma_{\text{coupled}} = F_C * \Gamma_C + F_D * \Gamma_D + \gamma_{PSB}, \qquad (2)$$

where Γ_0 is the uncoupled or bulk emission rate, and Γ_{coupled} is the cavity-coupled enhanced spontaneous emission rate. In our analysis, we neglect contributions from the A/B ZPL transitions of the SnV⁻, as the two higher energy transitions are suppressed in cryogenic conditions [8]. Therefore, in the uncoupled case, the total spontaneous emission rate is given by the sum of Γ_C , the C transition emission rate, Γ_D , the D transition emission rate, and γ_{PSB} , the rate of emission into the phonon side band (PSB). In the cavity-coupled case, F_C and F_D represent the Purcell factor that enhances the emission into the two orthogonal ZPL transitions. F_C and F_D can also be expressed as $F_C = F\cos(\theta)$ and $F_D = F\sin(\theta)$, respectively, to take into account the orthogonal polarizations of the C and D transitions. F is comprised of all shared factors which determine the Purcell factor for the two transitions, including Q/V ratio and emitter spatial position. θ represents the angular offset between the emitter transition dipole and the cavity mode polarization (Fig. 3e). We can also express θ in terms of ϕ , the global angular offset of the fabricated pattern with respect to the $\langle 100 \rangle$ crystal axis. Therefore we can write for the parallel cavity $\theta = 45 - \phi$, and for the angled

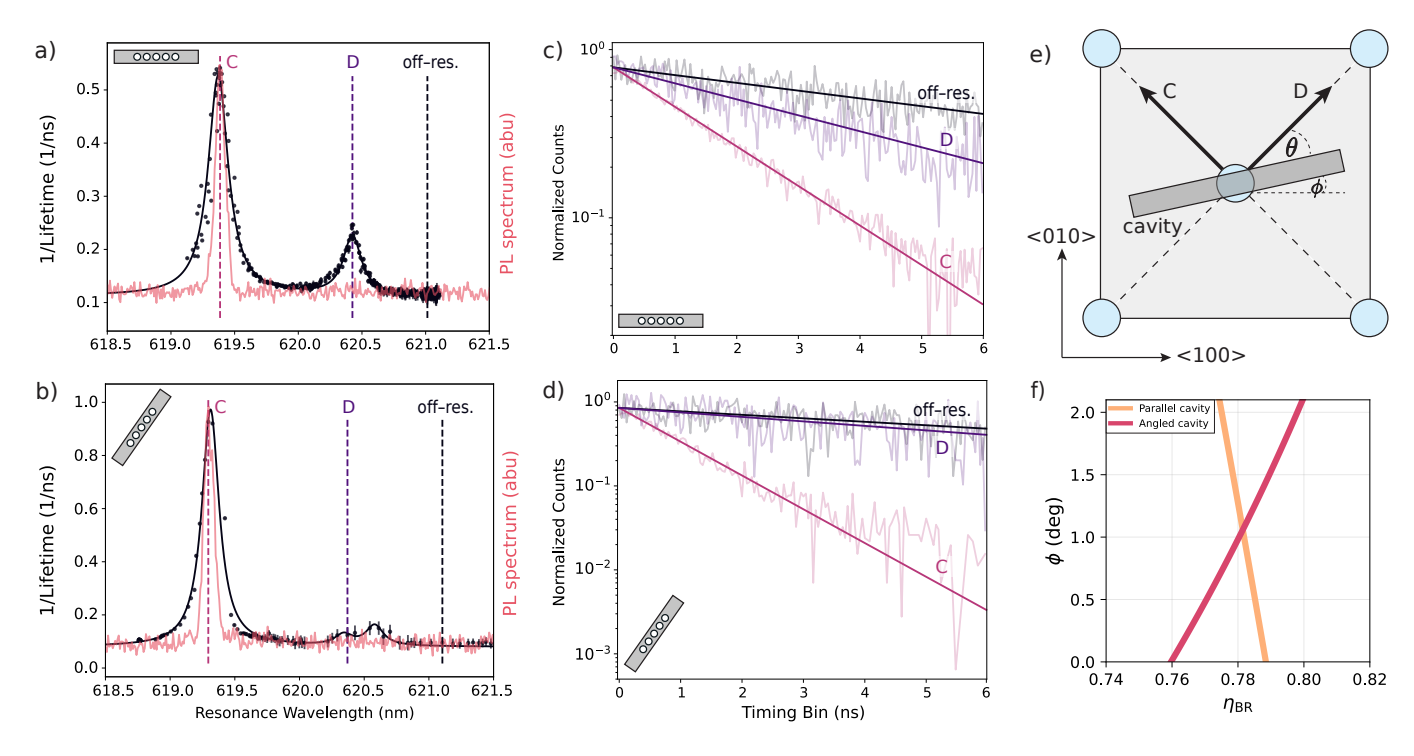


FIG. 3. Lifetime reduction and branching ratio analysis. (a) Spontaneous emission rate vs cavity resonance wavelength for the parallel device (black). The data are fit to a double Lorentzian model. The PL spectrum (red) is overlayed. We extract from this fit model the amplitude ratios $\zeta_C = 4.672$ and $\zeta_D = 1.985$. The three vertical dashed lines indicate the lifetime slices that are plotted separately, representing the traces with the C transition on resonance (pink), D transition on resonance (purple), and both transitions off resonance (black). (b) Spontaneous emission rate vs cavity resonance wavelength for the angled device (black). As in (a), the PL spectrum (red) is overlayed. For this device, we extract from this fit model the amplitude ratios $\zeta_C = 12.230$ and $\zeta_D = 1.514$. We note that due to filtering limitations, there are contributions from two separate emitters, and the data are thus fit to a quadruple Lorentzian model. The dashed lines indicate the lifetime slices of interest, as in panel (a). (c) Normalized lifetimes of the SnV⁻ with C/D transitions on and off resonance for the parallel device. We measure an off-resonance lifetime of 9.412 ± 0.09 ns. When the C(D) transition is on-resonance with the cavity, the lifetime is reduced to 1.847 ± 0.002 ns $(4.570 \pm 0.02$ ns). The lifetimes are fit to amplitude normalized and background corrected single exponential models. (d) Normalized lifetimes of the SnV⁻ with C/D transitions on and off resonance for the angled device. We measure an off-resonance lifetime of 10.507 ± 0.2 ns. When the C(D) transition is on-resonance, the lifetime is reduced to 1.079 ± 0.002 ns $(8.109 \pm 0.2 \text{ ns})$. The lifetimes are fit to amplitude normalized and background corrected single exponential models. We note that due to the contributions of a second emitter transition, at longer timescales, the data begins to deviate slightly from a single exponential mode. However, within the fitting range, the observed fluorescence lifetime is primarily dominated by a single decay timescale. (e) Schematic description of the cavity orientation with respect to the lattice sites and dipole moments of the C and D transitions. θ represents the angle between one of the dipoles and the cavity mode, and ϕ represents the collective fabrication angular offset from the diamond $\langle 100 \rangle$ lattice axis. (f) Solution of the analysis in Section II B 2, resulting in a branching ratio $\eta_{\rm BR}$ of 0.7815 and fabrication offset ϕ of 1.1 \pm 0.1 degrees.

cavity $\theta = 45 - (55 + \phi)$.

Dividing Γ_{coupled} by Γ_0 to analyze the emission enhancement ratios, we write:

$$\zeta = \frac{\Gamma_{\text{coupled}}}{\Gamma_0} = F_C * \frac{\Gamma_C}{\Gamma_0} + F_D * \frac{\Gamma_D}{\Gamma_0} + \frac{\gamma_{\text{PSB}}}{\Gamma_0}$$

$$= F_C * \eta_{\text{DW}} \eta_{\text{BR}}$$

$$+ F_D * \eta_{\text{DW}} (1 - \eta_{\text{BR}}) + (1 - \eta_{\text{DW}})$$
(3)

where $\eta_{\rm DW}=0.57$ is the Debye-Waller factor, or coherent ZPL proportion of total radiative emission [19]. $\eta_{\rm BR}$ is the branching ratio between transitions C and D. We are able to write two separate ratios, ζ_C and ζ_D , for when

the cavity is on resonance with transition C and D, respectively. For ratio ζ_C (ζ_D), we can set F_D (F_C) equal

We now recast these equations to solve for the Purcell factors:

$$F_C = F\cos(\theta) = \frac{\zeta_C + \eta_{\rm DW}\eta_{\rm BR} - 1}{\eta_{\rm DW}\eta_{\rm BR}}$$
(4)

$$F_C = F\cos(\theta) = \frac{\zeta_C + \eta_{\rm DW}\eta_{\rm BR} - 1}{\eta_{\rm DW}\eta_{\rm BR}}$$

$$F_D = F\sin(\theta) = \frac{\zeta_D + \eta_{\rm DW}(1 - \eta_{\rm BR}) - 1}{\eta_{\rm DW}(1 - \eta_{\rm BR})}$$

$$(5)$$

By taking the ratio of F_D to F_C , we can now write an equation for θ :

$$\tan(\theta) = \frac{\zeta_D + \eta_{\rm DW}(1 - \eta_{\rm BR}) - 1}{\zeta_C + \eta_{\rm DW}\eta_{\rm BR} - 1} * \frac{\eta_{\rm BR}}{1 - \eta_{\rm BR}}$$
 (6)

Using Eq. 6 with ζ_C and ζ_D determined from lifetime measurements, we vary $\eta_{\rm BR}$ and plot the resulting ϕ for both the parallel and angled cavity cases (Fig. 3f). By identifying the intersection between the two functions, we solve for $\phi = 1.1 \pm 0.1$, and the branching ratio $\eta_{BR} = 0.7815$, which is consistent with literature values [6, 14, 18] (Fig. 3f).

From these values we determine Purcell factors of $F_C=26.209\pm0.02$ and $F_D=5.123\pm0.05$ ($F_C=9.243\pm0.001$ and $F_D=8.910\pm0.0001$) for the angled (parallel) cavity. For the second emitter of the angled device, we can estimate Purcell factors of $F_C=1.048\pm0.005$ and $F_D=8.796\pm0.05$. We note that since the second emitter in the angled cavity demonstrates a larger Purcell factor for the D transition, we conclude that the emitter is oriented orthogonally to the other two emitters of study. Additional discussion regarding the second emitter is provided in Appendix D 3.

III. DISCUSSION

Our results highlight the importance of analyzing the lifetime reduction for both the C and D transitions. By explicitly modeling the collective spontaneous emission dynamics and accounting for the orthogonal polarizations of the C and D transition dipole moments, we are able to extract not only the individual Purcell factors of each transition, but also the intrinsic C/D branching ratio of the SnV^- .

This contrasts with prior work where Purcell factor is reported per SnV⁻ center and calculated by applying lump-sum correction factors [18, 20]. Furthermore, branching ratios were previously inferred from PL spectra or determined through quasi-resonant excitation [18, 21]. Distinguishing the Purcell enhancements of the C and D transitions provides a more faithful description of the underlying physics, which indicates the optimal emitter-cavity alignment for maximizing subsequent spin-state readout fidelity.

The asymmetry in cavity coupling between orthogonal transitions further serves as a sensitive probe of dipole orientation relative to the cavity field, allowing us to extract the angular alignment of the fabricated devices with respect to the crystal axes. If the collective lithography offset from the main lattice vector is known independently, for example via XRD measurements, the spontaneous emission equations for the C and D transitions in one cavity alone are sufficient to solve directly for both the branching ratio and Purcell factors. However, by investigating a second, angled cavity, we both validate our model and demonstrate the advantages of aligning the cavity mode polarization as closely as possible to the dipole orientation of a specific transition. Indeed, if the

angled cavity had been oriented 45° from the lattice vector rather than 55° , from our analysis we would expect complete suppression of one transition and further increased enhancement of the other. However, by allowing for a controlled 10° of angular misalignment, we ensure that we to observe some degree of coupling between both C and D transitions of the emitter, allowing for greater accuracy in our Purcell factor analysis.

IV. CONCLUSION

In this manuscript we report the fabrication of 1D photonic crystal cavity nanobeams from thin film diamond membranes. We achieve upwards of $\sim\!6000$ quality factors, and observe up to 10-fold PL enhancement from a select SnV⁻ when on resonance with the cavity mode. To accurately quantify our Purcell factors, we take time-resolved measurements and determine the optical lifetime reduction of the emitter. Despite optically filtering to isolate the C transition in collection, we also observe lifetime reduction when the cavity is on resonance with the D transition of the same emitter.

From this picture, we construct a model describing the spontaneous emission dynamics of the system. By studying the cavity-emitter coupling behavior of two separate devices—one roughly parallel and the other at $\sim 55^{\circ}$ to the diamond $\langle 100 \rangle$ lattice axis—we are able to extract a C/D branching ratio of $\eta_{\rm BR}=0.7815$ and a collective fabrication angular offset of $\phi=1.1\pm0.1^{\circ}$. Using the determined value of $\eta_{\rm BR}$, we determine Purcell factors of $F_C=9.243\pm0.001$ and $F_D=8.910\pm0.0001$ for the two transitions in the parallel cavity, and $F_C=26.209\pm0.01$ and $F_D=5.123\pm0.05$ for the angled device.

Our Purcell factor can be further increased through fabrication optimization, such as improving feature fidelity and minimizing device sidewall angles in the etch process (Appendix A 3). Furthermore, cavity-SnV $^-$ coupling can be improved through targeted and aligned implantation of Sn $^{2+}$ into the cavity mode volume [20]. Implantation density can be reduced for future devices in order to produce cavities with single color centers in the mode volume, while also cutting down on general implantation damage of the material.

Our fabricated sample is compatible with microwave spin driving experiments. By enhancing the $\mathrm{SnV^-}$ ZPL emission, readout fidelity of $\mathrm{SnV^-}$ spins can be significantly enhanced [9, 22]. Photon extraction can also be further improved by incorporating grating couplers or adiabatic tapers, which would enable color center addressing and photon collection in either transmission or reflection [14, 23–25]. These developments would enable near-unity fidelity of single shot readout of the electron spin in the $\mathrm{SnV^-}$, and pave the way for scalable quantum network nodes.

ACKNOWLEDGMENTS

This work was supported by the Department of Energy, Grant No. DE-SC0025295. This work was partially supported by Center for Integrated Nanotechnologies (CINT), a DOE Office of Science user facility jointly operated by Los Alamos and Sandia National Laboratories. We acknowledge the U.S. Department of Energy via the Q-NEXT Center Grant No. DOE 1F-60579 and We acknowledge the use of shared facilities of the UCSB Quantum Foundry through Q-AMASE-i program (NSF DMR-1906325). H.C.K. acknowledges support by the Burt and Deedee McMurtry Stanford Graduate Fellowship (SGF). Work was performed in part in the nano@Stanford labs, which are supported by the National Science Foundation as part of the National Nanotechnology Coordinated Infrastructure under award ECCS-2026822. Part of this work was performed at the Stanford Nano Shared Facilities (SNSF), supported by the National Science Foundation under award ECCS-2026822.

We would like to thank Lavendra Mandyam for helpful discussion in the clean room.

Appendix A: Thin Film and Device Fabrication

1. Diamond Thin Film Preparation

The thin film diamond material used for these experiments was prepared using the 'smart cut' technique and subsequent membrane exfoliation, as reported in [16, 17, 26, 27].

Electronic grade, single crystal diamond material was sourced from Element 6 and polished by Syntek to a miscut angle of 1°. The polishing induced strained layer is removed via RIE etching. A few microns is removed primarily by Ar/Cl etch chemistry, followed by a short (\sim 5 seconds) O₂ termination process to remove any Cl compounds on the surface. Helium ions (He²⁺) were implanted into the diamond with an implantation energy of 150 keV at a fluence of 5 \times 10¹⁶ ions/cm², and the chip was subsequently annealed at 850 °C in a high-vacuum chamber. The graphite layer formed from He²⁺ is \sim 100 nm thick and \sim 400 nm beneath the substrate surface [16].

Due to the high implantation energy and dosage, the material above the graphitization is rendered unsuitable for downstream color center formation and device fabrication. A new layer of diamond is thus grown homoepitaxially on the top surface using plasma-enhanced chemical vapor deposition (PECVD). Detailed information on the growth procedure is reported in [28].

To form tin vacancy centers, $\mathrm{Sn^{2+}}$ ions were implanted by a commercial vendor, Cutting Edge Ions, into the newly grown diamond layer with an implantation energy of 380 keV and a fluence of 2×10^{11} ions/cm². The Snimplanted chip was high-vacuum annealed at 400°C for 4 hours, 800°C for 4 hours, and then 1200°C for 2 hours

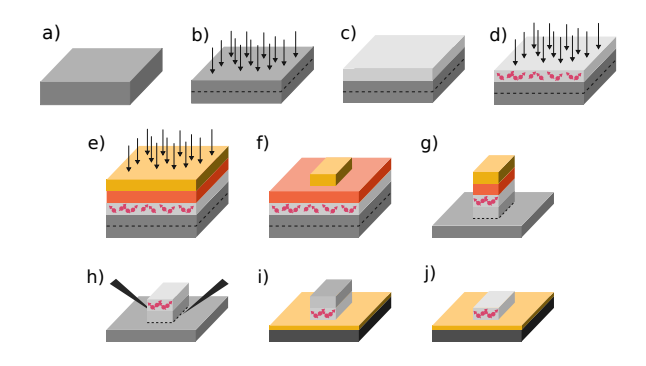


FIG. 4. Schematic of SnV⁻ implanted thin-film diamond preparation. The process starts with a bulk electronic grade diamond that is polished to a precise miscut angle (a). The sample is then heavily implanted with He²⁺ ions to form a vertically localized graphitized layer, around 400 nm below the sample surface (b). A pristine layer of single crystalline diamond is overgrown over the implantation damaged layer (c). $\rm Sn^{2+}$ is implanted $\sim\!90$ nm below the sample surface, and $\rm SnV^-$ centers are formed after high temperature, vacuum annealing (d). Any surface graphitization is removed via a tri-acid clean. A SiN hard mask is then deposited via CVD, and spun with photoresist (e). 200 μ m by 200 μ m squares are patterned by photolithography; these squares define the final size of each membrane (f). The membranes are defined in the bulk diamond by an anisotropic RIE etch (g). Individual membranes are then released via electrochemical etch (h), and bonded to a Si carrier wafer with HSQ (i). Finally, the film thickness is tuned to 180 nm via RIE etching (j).

to promote color center formation. The sample was then tri-acid cleaned at 250° C for an hour to remove any surface graphitization that may have developed during the anneal. Lastly, a 90 minute UV ozone treatment oxygen terminates the sample surface.

Membranes of size $200 \times 200~\mu m$ are patterned using photolithography and then released from the bulk using an electrochemical etch. The released membranes are then bonded damaged side up to Si carrier pieces via HSQ. Details on membrane exfoliation and transfer are outlined in [16]. The transferred membranes have a starting total thickness of $1\mu m$ and are thinned to the final desired thickness of 180 nm using reactive ion etching. We show a schematic of the full membrane preparation process in Fig. 4.

2. Photonic Crystal Fabrication Procedures

Photonic crystal fabrication begins with the prepared 180 nm thin film membranes bonded to Si. A thin ~ 25 nm ${\rm Al_2O_3}$ hard mask is deposited via thermal ALD. The sample is spun with ZEP and then the pattern exposed via e-beam lithography. The resist pattern is transferred into the hardmask with a BCl₃ chemistry ICP etch, and subsequently transferred into the diamond via a ${\rm Cl_2O_2/O_2}$ 2-step, cyclical ICP etch. The final devices

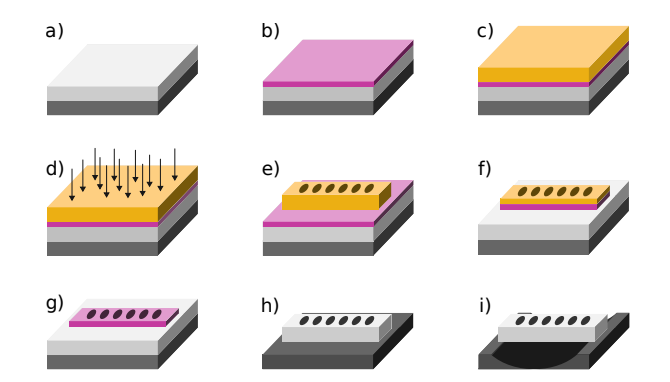


FIG. 5. Schematic of cavity fabrication procedure. The starting material consists of thin film diamond bonded to a Si handling wafer via HSQ (a). A thin Al_2O_3 had mask is deposited by ALD (b). The sample is spun with ZEP (c) and patterned via ebeam lithography (d, e). The resist pattern is transferred into the hardmask by ICP-RIE etching (f). Any remaining ZEP is then stripped (g), and the pattern transferred into the diamond membrane (g). Lastly, the devices are suspended by HF vapor and XeF₂ dry etching (i).

are then released via HF and XeF₂ vapor dry etches. We show this process schematically in Fig. 5.

3. Cavity Fabrication Yield and Fidelity

To account for fabrication uncertainties, the cavity lattice spacing was swept from 180 nm to 210 nm, in steps of 2.5 nm, for a total of 13 device designs. All other design parameters (beam width, hole diameter, cavity lattice tapering factor) were kept constant. From FDTD simulations, we expect resonance wavelengths to correspondingly vary from \sim 575 nm to \sim 684 nm, in steps of \sim 4 nm for each lattice spacing step. In Fig 7, we survey all devices across our sample to evaluate our fabrication yield and fidelity. Due to fabrication variation, we do not observe a clear trend between device lattice spacing and resonance wavelength. Quality factors seem to demonstrate a very slight increase with increased lattice spacings. We also note that we were unable to find any resonances for devices with the lowest four lattice spacings, ranging from 180 nm to 187.5 nm, most likely due to the overetching of cavity holes.

We evaluated the fabrication fidelity in detail for the two devices of study in the manuscript. Using Genisys ProSEM software, we analyze the tapered lattice spacings of the cavity holes (Fig. 6a,b). For the parallel device, we calculate a 2.013 ± 1 nm deviation from designed lattice spacings; for the angled device, we calculate 2.796 ± 3 nm deviation from designed spacings. Furthermore, we determine our device etch sidewall angle by fitting to both the top and bottom of the extracted beam width sigmoid. For the parallel device, we determine top (bottom) beam widths of 292.6 ± 15 nm $(358.6\pm14$ nm); for the angled cavity, we extract 304.9 ± 2 nm (337.3 ± 13)

nm). Given a consistent membrane thickness of 180 nm, we therefore determine sidewall angles of 10.389° and 5.143° , respectively, which are included in the simulations.

Appendix B: Characterization Setup

Here we describe the optical setup used for device and emitter studies (Fig. 8). The optical setup consists of two separate access arms, referred to in the manuscript as the 'PL' and 'cross polarized' paths. Access between the two paths are controlled via a motorized mirror (Thorlabs, MFF101).

The sample is housed in a Montana Instruments Cryostation s50 at 5K, and positioned via a tripe Attocube piezo stack (X101/Z100). The sample is addressed with a 100 μ m working distance, 100x magnification objective (Zeiss, EC Epiplan-NEOFLUOR 100x/0.9), which is mounted in a heater cryo-objective housing. The 4f confocal scanning microscope is constructed via a pair of 300 mm lenses(Thorlabs, AC254-300-A) and a galvo mirror (Newport, FSM-300-01). Polarization control is provided by the HWP (Thorlabs, AHWP10M-600).

In the cross polarized path, polarization filtering is provided by a polarizing beam splitter (Thorlabs, CCM1-PBS251). In the horizontally polarized collection path, the free space beam is coupled into a single mode (SM) fiber. In the horizontally polarized excitation arm, green and red wavelength splitting is achieved through a short-pass dichroic beamsplitter (Semrock, TSP01-561). The red excitation arm provides either resonant laser (Toptica, 1240 nm DL Pro, doubled via ADVR, frequency doubler) or broadband supercontinuum (superK, EVO EUL-10) light, coupled through a SM fiber. A Thorlabs, LP520-SF40 green diode laser is used for above band excitation. A HWP (Thorlabs, AHWP10M-600) and filter wheel is used to optimize and control power delivery, respectively.

In the PL path, we split green and red with via a longpass dicrhoic beamsplitter (Semrock, DMLP550). Subsequently, we split ZPL and PSB via a shortpass dichroics (Semrock, FF625-SDi01). Pulsed, 520 nm excitation is provided by a Thorlabs, GSL52A laser. Either resonant excitation or signal can be launched or collected from the ZPL path.

Collected signal is either routed to single photon counting modules (Excelitas, SPCM-AQRH-24) or a hybrid spectrometer (Acton, SpectraPro 2750 gratings and Andor, iDus416 CCD). For lifetime measurements, the parallel device lifetimes were collected on a Picoquant, Picoharp 300, while the angled device lifetimes were collected on a Swabian, Timetagger Ultra. Due to different timing resolution specs, the parallel device lifetimes were taken with 32 ps timing bins, and the angled device with 20 ps. During processing for the angled device, timing bins were further down-sampled to 40 ps. Pulse sequences are programmed and applied by a Swabian, Pulse Streamer

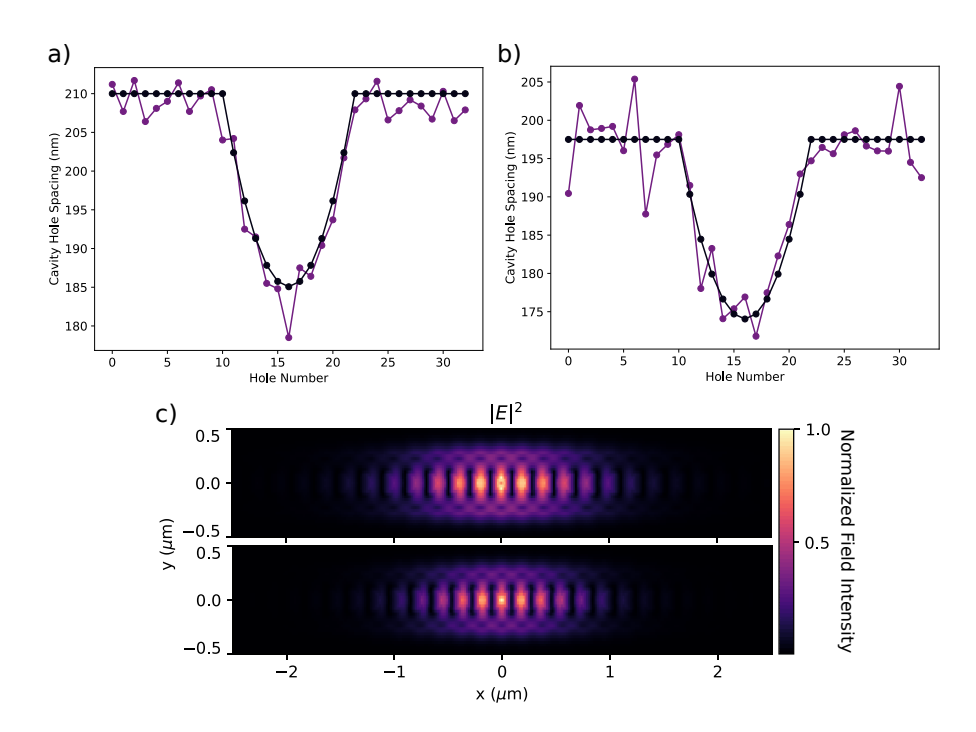


FIG. 6. Comparison of cavity lattice spacings. (a) Lattice spacing deviations for the parallel device. On average the cavity holes deviated by 2.013 ± 1 nm from designed positions. (b) Lattice spacing deviations for the angled device. Cavity holes deviated by 2.796 ± 3 nm from designed positions. (c) Simulated normalized electric field inside the cavity region of the parallel device (top) and angled device (bottom).

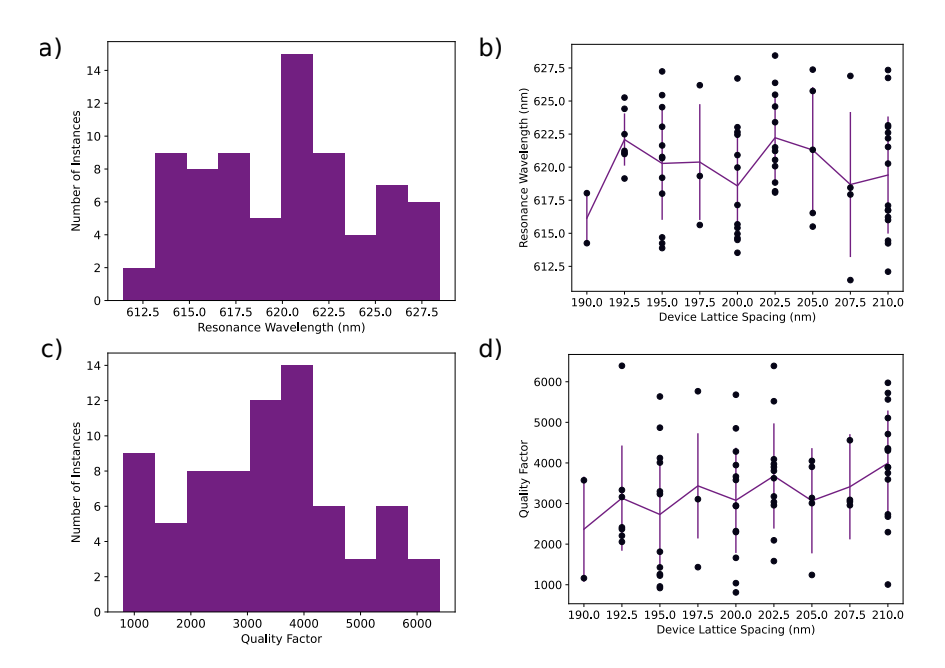


FIG. 7. Summary of cavity fabrication yield across the sample. (a) Histogram of resonance wavelengths for devices. Across all identified resonances, the average resonance wavelength is 620±4 nm. (b) Resonance wavelengths of all devices, summarized by the device lattice spacing. The black markers are data points from individual devices, while the purple line and errorbars indicate the average and standard deviation of of resonances wavelengths for devices of specific lattice spacings. From simulation we expect resonance wavelengths to red shift with increasing cavity lattice spacing; however, we do not observe a clear trend across our sample due to fabrication infidelities. (c) Histogram of quality factors for devices. Across all identified resonances, the average quality factor is 3335±1428. (d) Quality factors of all devices, summarized by the device lattice spacing. The black markers are data points from individual devices, while the purple line and errorbars indicate the average and standard deviation of of quality factors for devices of specific lattice spacings. Quality factors are expected to remain roughly constant across all device designs. For our sample, quality factor very slightly increases with increased lattice spacings.

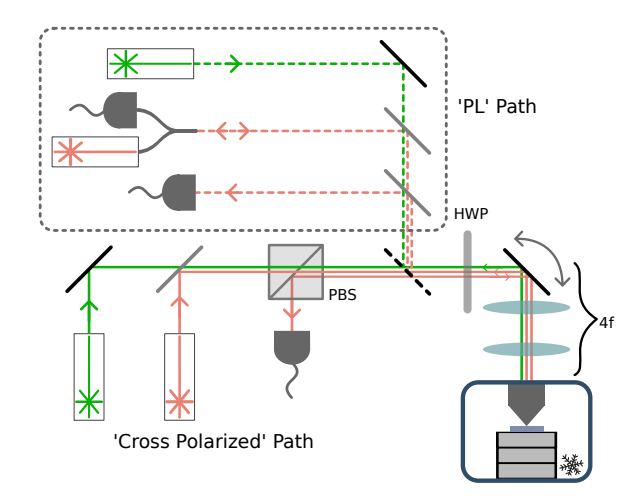


FIG. 8. Schematic of the measurement setup. The optical setup primarily consists of a home built, 4f confocal microscope with scanning enabled by a galvo mirror (4f). A half wave plate (HWP) is inserted right before the galvo mirror, allowing for simultaneous polarization rotation of all excitation and collection paths. The optical setup incorporates two discrete optical paths, referred to in this manuscript as the 'PL' and the 'cross polarized' paths. Access to either of these two paths are controlled via a flip mirror (dashed diagonal line). In the cross polarized path, the excitation is horizontally polarized, and collection vertically polarized, with the two paths mixed via a PSB. Green diode and broadband supercontinuum excitation are separately fed into the optics setup, with the two paths mixed via a shortpass dichroic beamsplitter. For the PL path, collection is first split between green and red via a longpass diocrhoic beamsplitter, and then further split between ZPL and PSB via a shortpass dichroic beamsplitter. When addressing emitters resonantly, the resonant laser is launched from the ZPL collection fiber coupler.

8/2. Pulsing and attenuation of the resonant excitation laser is provided by a G&H, Fiber-Q 633 nm AOM.

Fiber fluorescence from the green excitation sources are cleaned up with Thorlabs, FBH520-10 520/10 nm bandpass filters. Green scattering is further filtered from collection paths via Semrock, BLP01-594R 594 nm longpass filters. ZPL signal is isolated through Semrock, FBP01-620/14 620/14 nm bandpass filters. Filtering for isolating single SnV $^-$ transition lines was achieved using a custom ordered Rapid Spectral Solutions, 622/0.3 nm bandpass filter, designed to have ~ 5 nm of tuning range.

Appendix C: Resonant Color Center Addressing

Prior to patterning photonic devices, optical characterization was performed to verify formation of color centers in the thin film material. Using 4f confocal microscopy, 2D PL spatial maps were obtained using an above-resonant (green, 520 nm) diode laser and bright spots probed with spectroscopy (Fig. 9a). From Fig. 9b, the large density of SnV⁻s formed is evident from the PL spectra. This high emitter density is also evident when

resonantly addressing the SnV $^-$ candidates. Within ~ 40 GHz of laser scanning range, we can address on the order of 3-4 color centers (Fig. 9d).

To study the coherence of these color centers, we perform PLE spectroscopy via the PL optical path. We excite the SnV⁻ with alternating pulsed green and red excitation; SPCM collection is gated with red excitation to reduce signal background. The full pulse sequence is 20 μ s, with 4 μ s of green excitation, 4 μ s of offset, and 12 μ s of red excitation and SPCM collection. Pulsing for the green diode is provided by direct modulation of the laser diode, while pulsing for the red is provided by an AOM. The red laser is scanned across $\sim 40~\mathrm{GHz}$ with a frequency of 0.2 Hz. We are also able to identify SnV^- transitions with down to a ~ 320 MHz linewidth, stable for ~ 30 minutes (Fig. 9e). Estimating from the off-resonance lifetimes as reported in Section IIB2, the Fourier limit linewidth would be on the order of 100 MHz. However, color centers of higher coherence in both bulk and thin-film diamond have been reported [29, 30]. We attribute our measured linewidth to insufficient optimization of PLE experimental parameters, lack of an exhaustive survey of emitters, and the high Sn²⁺implantation density.

Post-device fabrication, we first attempt PLE for the emitter of study in the parallel device. Although the PLE is consistent over ~30 minutes, the emitter demonstrates significant linewidth broadening, with an averaged linewidth of 15.382 pm (Fig. 10a,d). We also probe a secondary emitter in the device which is much more weakly coupled to the cavity mode. This emitter instead demonstrates an averaged linewdith of 1.368 pm; the PLE signal is stable over ~30 minutes. The further linewidth broadening of the emitters in fabricated devices likely stemmed from the proximity of etched surfaces. To mitigate these effects, inspiration can be taken from efforts to improve near-surface NV coherence via surface passivation or chemical termination [31, 32].

Appendix D: Extended Data

1. Cavity Mode Polarization Dependence

To verify that the nanobeam cavity modes are linearly polarized, we measure the angular dependence of the reflectivity amplitude by rotating the HWP. The angular dependence demonstrates sinusoidal behavior with a periodicity of ${\sim}45^{\circ}$, indicating a linearly polarized mode (Fig. 11 [33]. The amplitude modulation of the sinusoidal trend is likely due to slight shifts in beam positioning introduced by HWP rotation.

2. Angled Cavity and PL Characterization

When measured in cross polarized reflectivity, the angled device yields a quality factor of 3942.350 ± 0.0003 ,

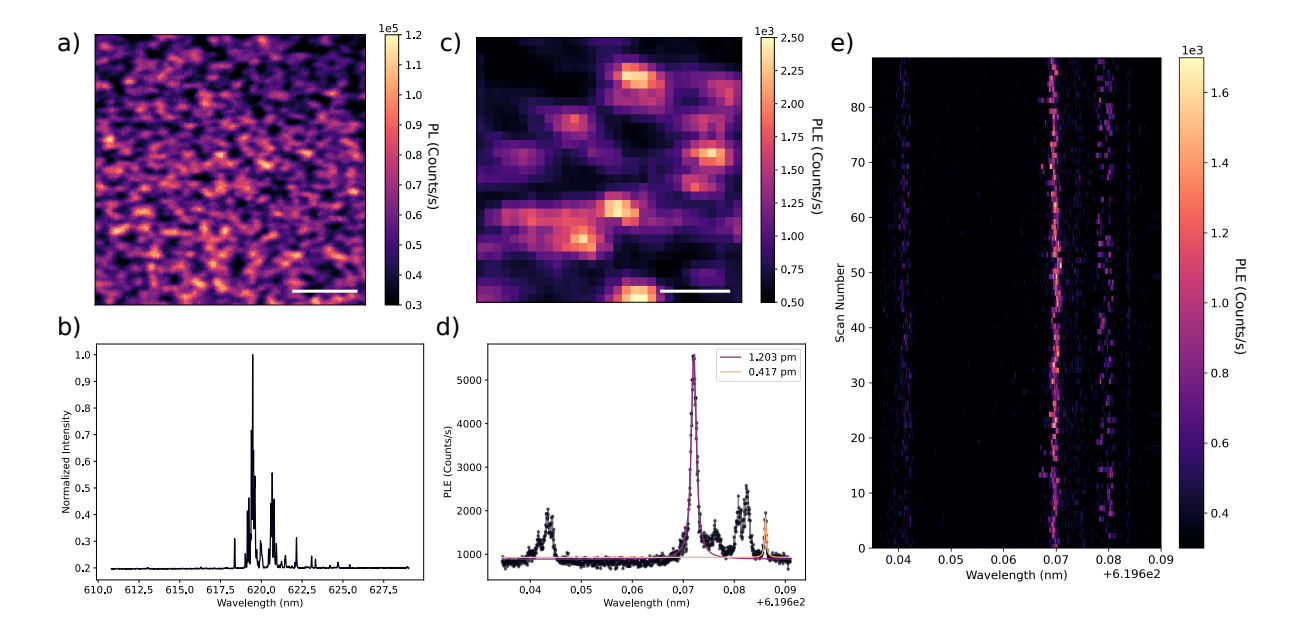


FIG. 9. Color center characterization in thin film, pre device fabrication. (a) PL confocal scan of the thin film pre device fabrication. The density of bright spots indicates the larger number of SnV⁻s formed during implantation. The scale bar indicates 3μ m. (b) Representative PL spectrum for a probed emitter cluster, demonstrating SnV⁻ formation density. (c) PLE confocal scan. A full PLE scan is taken and count rates summed per pixel of the 2D spatial map. All emitters which show up are addressable within the laser scanning range of \sim 40 GHz. The scale bar indicates 1μ m. (d) Averaged PLE. Two representative transitions are fit with a Lorentzian model to estimate the linewidths. The more prominent transition demonstrates a 1.236 pm or \sim 1 GHz linewidth. The other transition demonstrates a 0.417 pm or \sim 320 MHz linewidth, around 3 times larger that our estimated Fourier limit of \sim 100 MHz. (e) PLE traces over 30 minutes. The stability of the PLE indicates prolonged SnV⁻ coherence in the thin film.

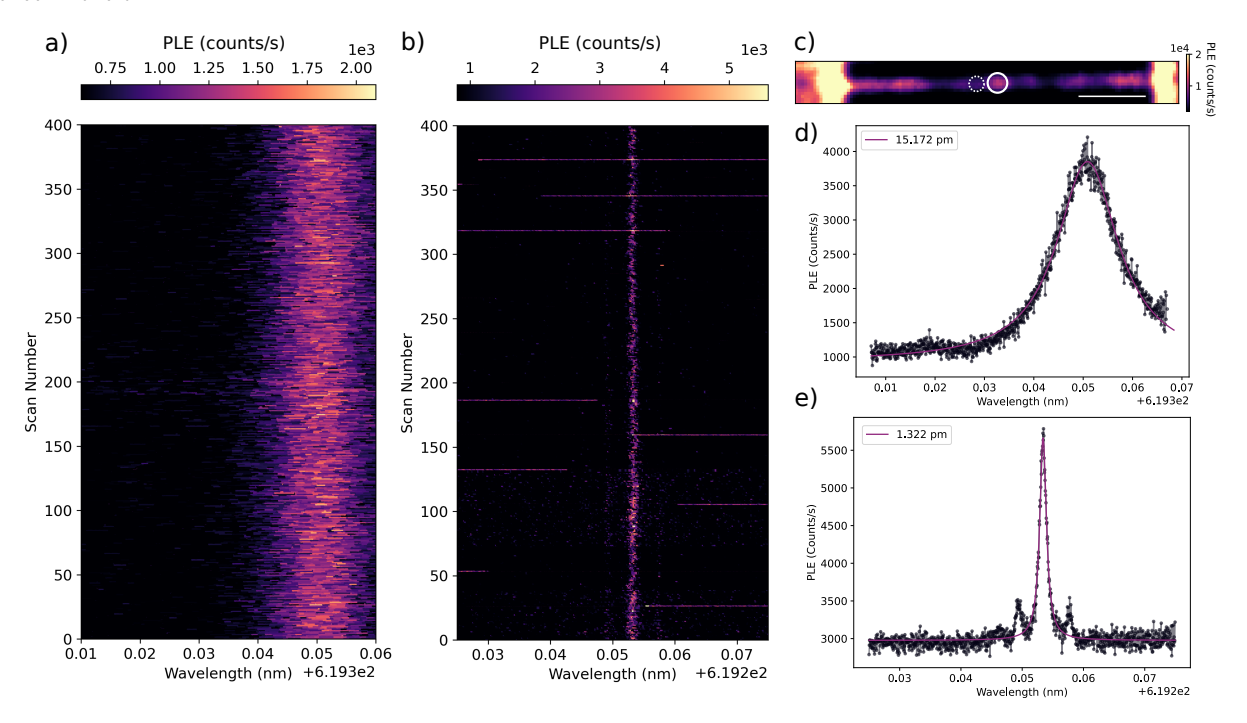


FIG. 10. Resonant color center addressing in fabricated devices. (a) PLE traces for ~30 minutes on the color center of focus in the parallel device. (b) PLE traces for ~30 minutes for a secondary emitter in the parallel device. (c) PLE confocal scan of the parallel device. The main emitter of study in this manuscript is indicated by the solid circle, while the dashed circle notates the secondary emitter of study. (d) Averaged PLE of the traces from (a). A Lorentzian fit yields a linewidth of 15.382 pm. (e) Averaged PLE of the traces from (b). A Lorentzian fit yields a 1.386 pm linewidth. We note that the side lobes of the mean PLE peak feature was due to laser instability and multimodedness.

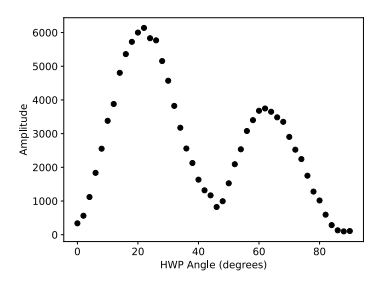


FIG. 11. Angular dependence of cavity reflectivity amplitude. The periodicity of the oscillatory behavior is $\sim 45^{\circ}$, indicating a linearly polarized mode.

determined through a Fano fit on a background corrected broadband spectrum (Fig. 12). In Fig. 13, we also present the PL confocal scan of the angled device of interest. Similar to with the parallel cavity, the high implantation dose resulted in a cluster of 2-3 emitters coupled to the cavity mode. The most strongly enhanced transitions demonstrates a ~ 2.25 -fold PL enhancement when on resonance with the cavity (Fig. 13). We note that this figure illustrates the necessity of lifetime reduction measurements for rigorously determining Purcell factors in a cavity QED system.

3. Secondary Emitter in the Angled Cavity Mode

In this section we discuss the behavior of the second emitter in the angled cavity mode. Due to the bandwidth of the tunable optical filter (~ 0.3 nm), a small contribution from a second emitter is collected during lifetime measurements for the angled cavity. This contribution is visible when a PL spectrum is taken of the optically filtered collection spot with long integration times (Fig. 14a).

When the C(D) transition is on resonance, the secondary emitter demonstrates a reduced lifetime of 8.008 ± 0.07 ns $(6.659\pm0.2$ ns). By extracting the amplitude fit parameters of the quadruple Lorentzian model, we determine amplitude ratios of $\zeta_C=1.022\pm0.002$ and $\zeta_D=1.971\pm0.006$. Given that the D transition demonstrates greater lifetime reduction than the C transition, we conclude that this secondary emitter is orthogonal in orientation to the other two SnV⁻s of study, and therefore the angular offset between the emitter transition dipole and cavity mode is given by $\theta=45-(55+\phi)+90$.

Accounting for this second emitter, we can once again use Eq. 6 to solve for $\eta_{\rm BR}$ and ϕ . From Fig. 14c, we see that the three trend lines fail to fully intersect. This discrepancy is likely due to increased fitting errors, stemming from reduced SNR per lifetime measurement for this more weakly coupled emitter. Therefore, we instead minimize the averaged pairwise differences between for all trend lines, identifying the optimal value $\eta_{\rm BR}=0.7815$, identical to that determined in Section II B 3. Therefore, we determine that this secondary emitter demonstrates Purcell factors of 1.048 ± 0.005 and 8.796 ± 0.05 , for the C and D transitions, respectively.

H. J. Kimble, The quantum internet, Nature 453, 1023 (2008).

^[2] D. D. Awschalom, R. Hanson, J. Wrachtrup, and B. B. Zhou, Quantum technologies with optically interfaced solid-state spins, Nature Photonics 12, 516 (2018).

^[3] M. Atatüre, D. Englund, N. Vamivakas, S.-Y. Lee, and J. Wrachtrup, Material platforms for spin-based photonic quantum technologies, Nature Reviews Materials 3, 38 (2018).

^[4] M. Pompili, S. L. Hermans, S. Baier, H. K. Beukers, P. C. Humphreys, R. N. Schouten, R. F. Vermeulen, M. J. Tiggelman, L. dos Santos Martins, B. Dirkse, et al., Realization of a multinode quantum network of remote solid-state qubits, Science 372, 259 (2021).

^[5] H. Bernien, B. Hensen, W. Pfaff, G. Koolstra, M. S. Blok, L. Robledo, T. H. Taminiau, M. Markham, D. J. Twitchen, L. Childress, et al., Heralded entanglement between solid-state qubits separated by three metres, Nature 497, 86 (2013).

^[6] G. Thiering and A. Gali, Ab initio magneto-optical spectrum of group-iv vacancy color centers in diamond, Physical Review X 8, 021063 (2018).

^[7] C. M. Knaut, A. Suleymanzade, Y.-C. Wei, D. R. As-

sumpcao, P.-J. Stas, Y. Q. Huan, B. Machielse, E. N. Knall, M. Sutula, G. Baranes, *et al.*, Entanglement of nanophotonic quantum memory nodes in a telecom network, Nature **629**, 573 (2024).

^[8] T. Iwasaki, Y. Miyamoto, T. Taniguchi, P. Siyushev, M. H. Metsch, F. Jelezko, and M. Hatano, Tin-vacancy quantum emitters in diamond, Phys. Rev. Lett. 119, 253601 (2017).

^[9] E. I. Rosenthal, C. P. Anderson, H. C. Kleidermacher, A. J. Stein, H. Lee, J. Grzesik, G. Scuri, A. E. Rugar, D. Riedel, S. Aghaeimeibodi, et al., Microwave spin control of a tin-vacancy qubit in diamond, Physical Review X 13, 031022 (2023).

^[10] E. I. Rosenthal, S. Biswas, G. Scuri, H. Lee, A. J. Stein, H. C. Kleidermacher, J. Grzesik, A. E. Rugar, S. Aghaeimeibodi, D. Riedel, et al., Single-shot readout and weak measurement of a tin-vacancy qubit in diamond, Physical Review X 14, 041008 (2024).

^[11] A. E. Rugar, C. Dory, S. Aghaeimeibodi, H. Lu, S. Sun, S. D. Mishra, Z.-X. Shen, N. A. Melosh, and J. Vučković, Narrow-linewidth tin-vacancy centers in a diamond waveguide, ACS Photonics 7, 2356 (2020).

^[12] A. E. Rugar, S. Aghaeimeibodi, D. Riedel, C. Dory,

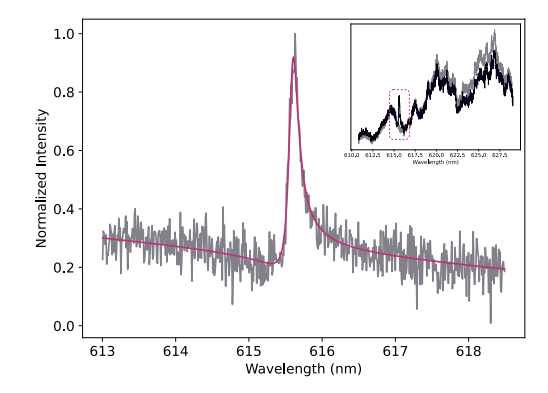


FIG. 12. Angled cavity quality factor characterization. The full broacband relfectivity spectra for the resonance and background are shown in the inset. The fitted region is indicated by the dashed line. As with the parallel device, the resonance is fit to a Fano model.

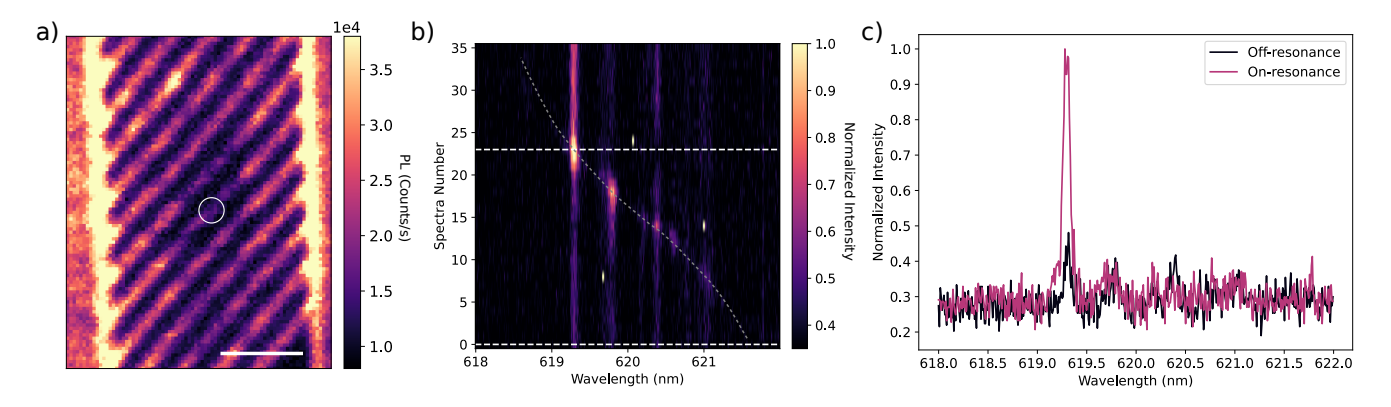


FIG. 13. Angled cavity PL confocal scan and cavity enhancement. (a) PL confocal scan of the angled device studied in this manuscript. The emitter cluster of focus is indicated by the white circle. The scale bar indicates 3μ m. (b) PL enhancement of the SnV⁻s located in the angled device cavity mode. The spectra for the transition of interest on and off resonance are indicated by the white dahsed lines. The grey dashed line is a guide for the eye of the cavity resonance wavelength. (c) PL spectra of the two spectra of interest. From comparing the transition amplitude on and off resonance, we estimate a 2.5-fold PL enhancement from gas tuning.

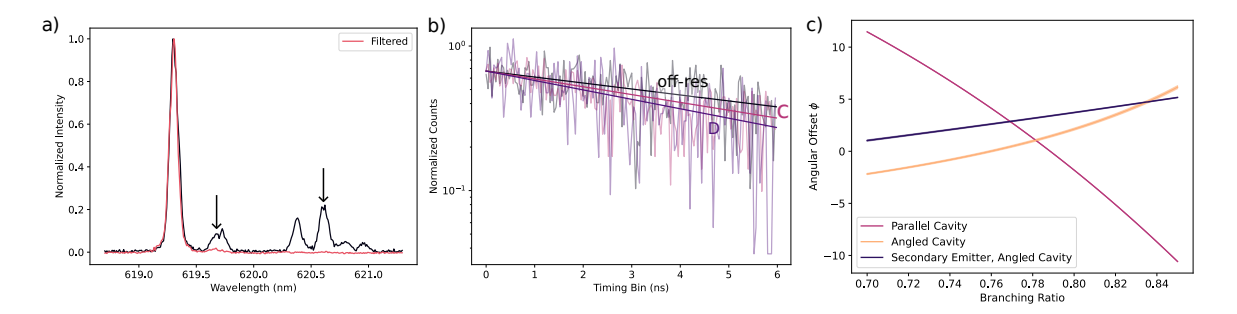


FIG. 14. Lifetime reduction of secondary emitter. (a) Filtered and unfiltered PL spectra of the collection spot for the angled device. Both are normalized in order to show degree of suppression of other transitions by the tunable filter. The arrows indicate the estimated C and D transitions of the second emitter. In the filtered spectrum, it is evident that a small contribution of the secondary C transition remains. (b) Lifetime reduction for when the secondary emitter is on/off resonance. The C transition demonstrates a reduced lifetime of 8.008 ± 0.7 ns, and D demonstrates a reduced lifetime of 6.659 ± 0.2 ns. The off resonance lifetime is 10.507 ± 0.2 ns. (c) Solution for Purcell analysis for three emitters. Although the three functions fail to intersect, minimizing the average difference yields $\eta_{\rm BR} = 0.7815$, consistent with the value calculated in Section II B 3.

- H. Lu, P. J. McQuade, Z. X. Shen, N. A. Melosh, and J. Vučković, Quantum photonic interface for tin-vacancy centers in diamond, Physical Review X 11 (2021).
- [13] K. Kuruma, B. Pingault, C. Chia, D. Renaud, P. Hoff-mann, S. Iwamoto, C. Ronning, and M. Lončar, Coupling of a single tin-vacancy center to a photonic crystal cavity in diamond, Applied Physics Letters 118, 230601 (2021).
- [14] M. Pasini, N. Codreanu, T. Turan, A. Riera Moral, C. F. Primavera, L. De Santis, H. K. C. Beukers, J. M. Brevoord, C. Waas, J. Borregaard, and R. Hanson, Nonlinear quantum photonics with a tin-vacancy center coupled to a one-dimensional diamond waveguide, Phys. Rev. Lett. 133, 023603 (2024).
- [15] S. W. Ding, M. Haas, X. Guo, K. Kuruma, C. Jin, Z. Li, D. D. Awschalom, N. Delegan, F. J. Heremans, A. A. High, and M. Loncar, High-q cavity interface for color centers in thin film diamond, Nature Communications 15 (2024).
- [16] H. Oh, V. Dharod, C. Padgett, L. B. Hughes, J. Venkatraman, S. Parthasarathy, E. Osipova, I. Hedgepeth, J. V. Cady, L. Basso, et al., A spin-embedded diamond optomechanical resonator with mechanical quality factor exceeding one million, arXiv preprint arXiv:2508.05906 (2025).
- [17] X. Guo, N. Delegan, J. C. Karsch, Z. Li, T. Liu, R. Shreiner, A. Butcher, D. D. Awschalom, F. J. Heremans, and A. A. High, Tunable and transferable diamond membranes for integrated quantum technologies, Nano Letters 21, 10392 (2021).
- [18] A. E. Rugar, C. Dory, S. Sun, and J. Vučković, Characterization of optical and spin properties of single tinvacancy centers in diamond nanopillars, Phys. Rev. B 99, 205417 (2019).
- [19] J. Görlitz, D. Herrmann, G. Thiering, P. Fuchs, M. Gandil, T. Iwasaki, T. Taniguchi, M. Kieschnick, J. Meijer, M. Hatano, A. Gali, and C. Becher, Spectroscopic investigations of negatively charged tin-vacancy centres in diamond, New Journal of Physics 22, 013048 (2020).
- [20] A. Sipahigil, R. E. Evans, D. D. Sukachev, M. J. Burek, J. Borregaard, M. K. Bhaskar, C. T. Nguyen, J. L. Pacheco, H. A. Atikian, C. Meuwly, R. M. Camacho, F. Jelezko, E. Bielejec, H. Park, M. Lončar, and M. D. Lukin, An integrated diamond nanophotonics platform for quantum-optical networks, Science 354, 847 (2016).
- [21] J. L. Zhang, S. Sun, M. J. Burek, C. Dory, Y.-K. Tzeng, K. A. Fischer, Y. Kelaita, K. G. Lagoudakis, M. Radulaski, Z.-X. Shen, N. A. Melosh, S. Chu, M. Lončar, and J. Vučković, Strongly cavity-enhanced spontaneous emission from silicon-vacancy centers in diamond, Nano Letters 18, 1360 (2018).
- [22] R. E. Evans, M. K. Bhaskar, D. D. Sukachev, C. T. Nguyen, A. Sipahigil, M. J. Burek, B. Machielse, G. H. Zhang, A. S. Zibrov, E. Bielejec, H. Park, M. Lončar, and M. D. Lukin, Photon-mediated interactions between quantum emitters in a diamond nanocavity, Science 362, 662 (2018).
- [23] M. J. Burek, C. Meuwly, R. E. Evans, M. K. Bhaskar, A. Sipahigil, S. Meesala, B. Machielse, D. D. Sukachev, C. T. Nguyen, J. L. Pacheco, E. Bielejec, M. D. Lukin, and M. Lončar, Fiber-coupled diamond quantum nanophotonic interface, Phys. Rev. Appl. 8, 024026 (2017).
- [24] R. A. Parker, J. Arjona Martínez, K. C. Chen, A. M.

- Stramma, I. B. Harris, C. P. Michaels, M. E. Trusheim, H. Appel, P. Martin, R. Carola M., W. G., D. Englund, and M. Atatüre, A diamond nanophotonic interface with an optically accessible deterministic electronuclear spin register, Nature Photonics 18, 156–161 (2024).
- [25] C. T. Nguyen, D. D. Sukachev, M. K. Bhaskar, B. Machielse, D. S. Levonian, E. N. Knall, P. Stroganov, R. Riedinger, H. Park, M. Lončar, and M. D. Lukin, Quantum network nodes based on diamond qubits with an efficient nanophotonic interface, Phys. Rev. Lett. 123, 183602 (2019).
- [26] J. C. Lee, A. P. Magyar, D. O. Bracher, I. Aharonovich, and E. L. Hu, Fabrication of thin diamond membranes for photonic applications, Diamond and related materials 33, 45 (2013).
- [27] Y. Li, F. A. Gerritsma, S. Kurdi, N. Codreanu, S. Gröblacher, R. Hanson, R. Norte, and T. van der Sar, A fiber-coupled scanning magnetometer with nitrogenvacancy spins in a diamond nanobeam, ACS Photonics 10, 1859 (2023).
- [28] L. B. Hughes, Z. Zhang, C. Jin, S. A. Meynell, B. Ye, W. Wu, Z. Wang, E. J. Davis, T. E. Mates, N. Y. Yao, et al., Two-dimensional spin systems in pecvd-grown diamond with tunable density and long coherence for enhanced quantum sensing and simulation, APL Materials 11 (2023).
- [29] M. E. Trusheim, B. Pingault, N. H. Wan, M. Gündoğan, L. De Santis, R. Debroux, D. Gangloff, C. Purser, K. C. Chen, M. Walsh, J. J. Rose, J. N. Becker, B. Lienhard, E. Bersin, I. Paradeisanos, G. Wang, D. Lyzwa, A. R.-P. Montblanch, G. Malladi, H. Bakhru, A. C. Ferrari, I. A. Walmsley, M. Atatüre, and D. Englund, Transformlimited photons from a coherent tin-vacancy spin in diamond, Phys. Rev. Lett. 124, 023602 (2020).
- [30] X. Guo, A. M. Stramma, Z. Li, W. G. Roth, B. Huang, Y. Jin, R. A. Parker, J. Arjona Martínez, N. Shofer, C. P. Michaels, C. P. Purser, M. H. Appel, E. M. Alexeev, T. Liu, A. C. Ferrari, D. D. Awschalom, N. Delegan, B. Pingault, G. Galli, F. J. Heremans, M. Atatüre, and A. A. High, Microwave-based quantum control and coherence protection of tin-vacancy spin qubits in a straintuned diamond-membrane heterostructure, Phys. Rev. X 13, 041037 (2023).
- [31] S. Sangtawesin, B. L. Dwyer, S. Srinivasan, J. J. Allred, L. V. H. Rodgers, K. De Greve, A. Stacey, N. Dontschuk, K. M. O'Donnell, D. Hu, D. A. Evans, C. Jaye, D. A. Fischer, M. L. Markham, D. J. Twitchen, H. Park, M. D. Lukin, and N. P. de Leon, Origins of diamond surface noise probed by correlating single-spin measurements with surface spectroscopy, Phys. Rev. X 9, 031052 (2019).
- [32] R. Kumar, S. Mahajan, F. Donaldson, S. Dhomkar, H. J. Lancaster, C. Kalha, A. A. Riaz, Y. Zhu, C. A. Howard, A. Regoutz, and J. J. L. Morton, Stability of near-surface nitrogen vacancy centers using dielectric surface passivation, ACS Photonics 11, 1244 (2024).
- [33] Y. Gong and J. Vučković, Photonic crystal cavities in silicon dioxide, Applied Physics Letters 96, 031107 (2010).
- [34] J. M. Brevoord, L. D. Santis, T. Yamamoto, M. Pasini, N. Codreanu, T. Turan, H. K. Beukers, C. Waas, and R. Hanson, Heralded initialization of charge state and optical-transition frequency of diamond tin-vacancy centers, Physical Review Applied 21 (2024).
- [35] K. Ikeda, Y. Chen, P. Wang, Y. Miyamoto, T. Taniguchi, S. Onoda, M. Hatano, and T. Iwasaki, Charge state tran-

- sition of spectrally stabilized tin-vacancy centers in diamond, ACS Photonics 12, 2972 (2025).
- [36] C. Hepp, T. Müller, V. Waselowski, J. N. Becker, B. Pingault, H. Sternschulte, D. Steinmüller-Nethl, A. Gali, J. R. Maze, M. Atatüre, and C. Becher, Electronic structure of the silicon vacancy color center in diamond, Phys. Rev. Lett. 112, 036405 (2014).
- [37] S. Aghaeimeibodi, D. Riedel, A. E. Rugar, C. Dory, and
- J. Vučković, Electrical tuning of tin-vacancy centers in diamond, Phys. Rev. Appl. ${\bf 15},\,064010$ (2021).
- [38] D. S. Levonian, R. Riedinger, B. Machielse, E. N. Knall, M. K. Bhaskar, C. M. Knaut, R. Bekenstein, H. Park, M. Lončar, and M. D. Lukin, Optical entanglement of distinguishable quantum emitters, Phys. Rev. Lett. 128, 213602 (2022).